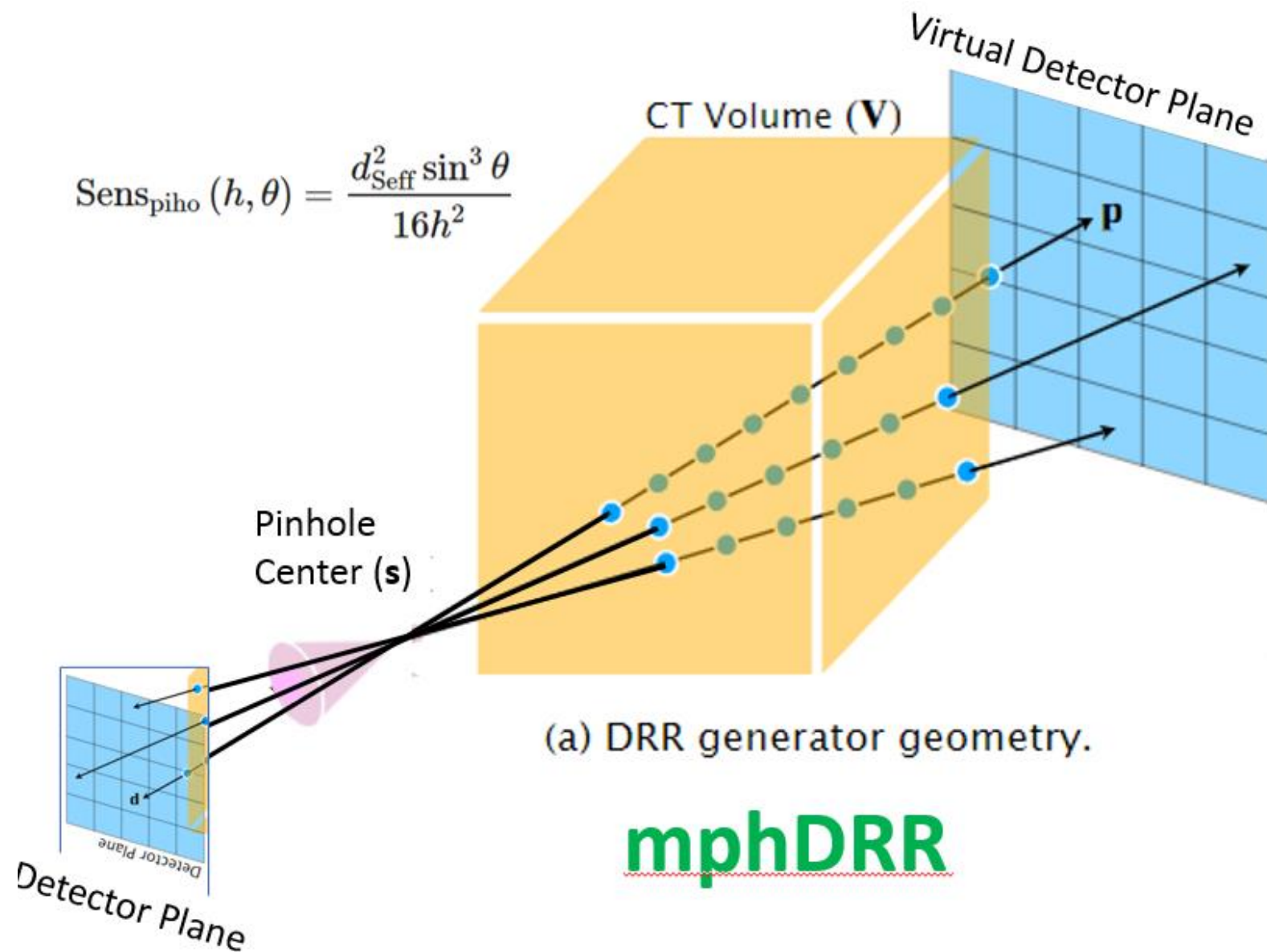


mphDRR Design and Literature Review

Bill Worstell
PicoRad->MGH
12/22/2023



mphDRR

Gopalakrishnan, V. and Golland, P., 2022, September. [Fast auto-differentiable digitally reconstructed radiographs for solving inverse problems in intraoperative imaging](#). In *Workshop on Clinical Image-Based Procedures* (pp. 1-11). Cham: Springer Nature Switzerland.

mphSPECT differs from X-ray forward projection, requiring multiplication by reciprocal squared distance from pinhole to source voxel

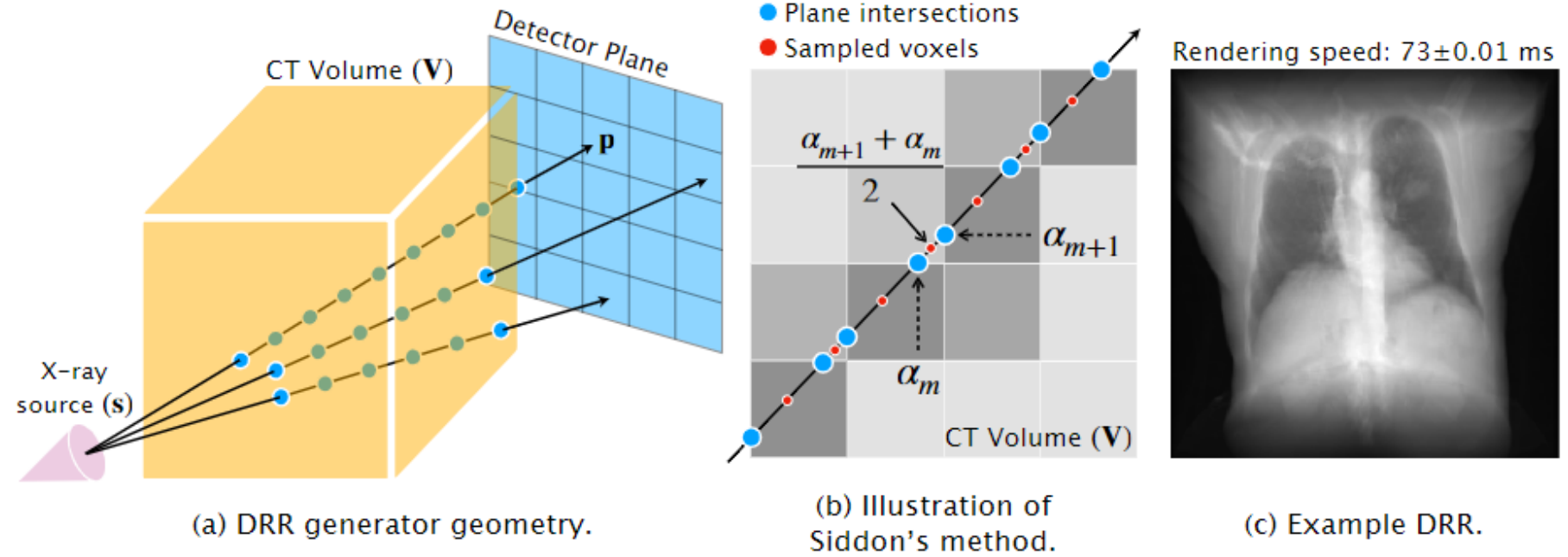
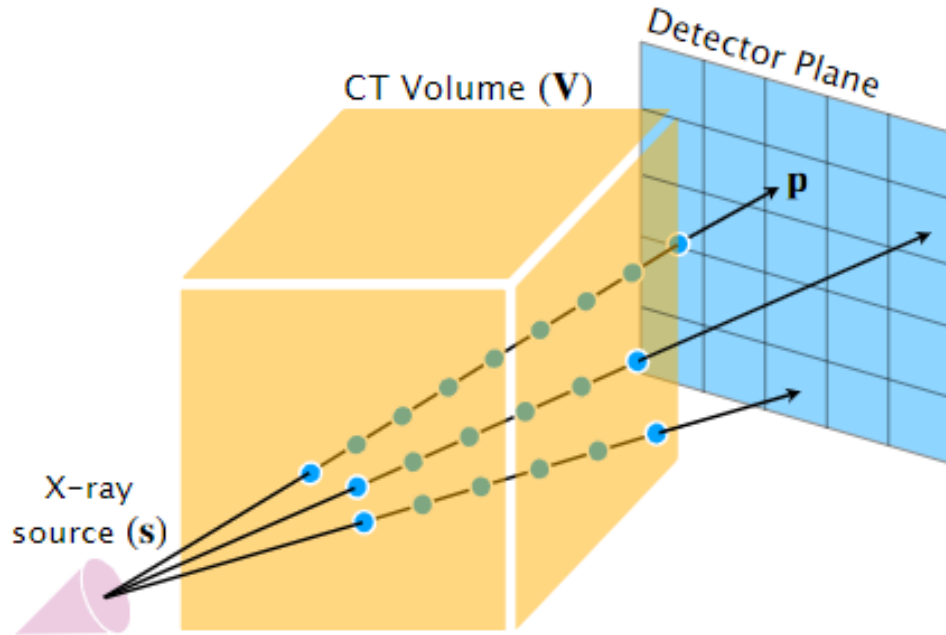


Fig. 1. DRR synthesis. (a) We assume an idealized model of a projectional radiography imaging system: X-ray beams are emitted with a fixed initial energy from a point source $\mathbf{s} \in \mathbb{R}^3$, beam energy diminishes as the X-rays travel through the CT volume \mathbf{V} , and energy in the attenuated beams is measured when the X-rays hit a point on the detector $\mathbf{p} \in \mathbb{R}^3$, producing the DRR. (b) In Siddon's method, the image location value at \mathbf{p} is a weighted average of the intensities of the voxels through which the ray passes, where the weight is the length of the ray's intersection with the voxel. The values α_m and α_{m+1} parameterize the intersection of the ray with two adjacent planes, and the midpoint $\frac{\alpha_{m+1} + \alpha_m}{2}$ identifies the current voxel through which the ray is passing. (c) Our vectorized Siddon's method generates a 200×200 DRR in $72.7 \text{ m sec} \pm 10 \mu \text{ sec}$ on an NVIDIA GeForce RTX 2080 Ti.

Xray DRR



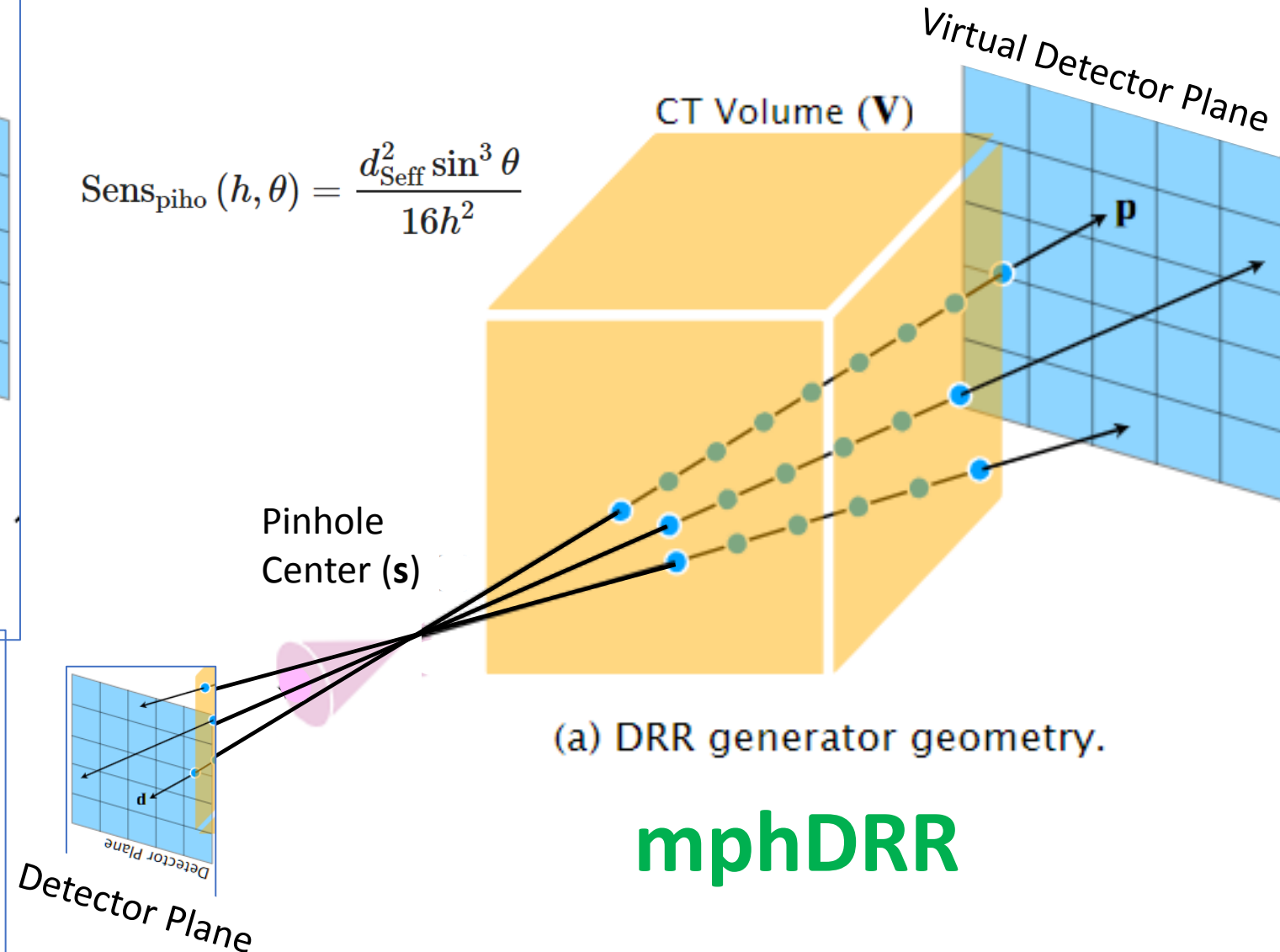
(a) DRR generator geometry.

Gopalakrishnan, V. and Golland, P., 2022, September. [Fast auto-differentiable digitally reconstructed radiographs for solving inverse problems in intraoperative imaging](#).

In *Workshop on Clinical Image-Based Procedures* (pp. 1-11). Cham: Springer Nature Switzerland.

Virtual Detector Mapping for Infinitesimal Pinhole

$$\text{Sens}_{\text{piho}}(h, \theta) = \frac{d_{\text{Seff}}^2 \sin^3 \theta}{16h^2}$$



(a) DRR generator geometry.

mphDRR

Van Audenhaege, K., Van Holen, R., Vandenberghe, S., Vanhove, C., Metzler, S.D. and Moore, S.C., 2015. [Review of SPECT collimator selection, optimization, and fabrication for clinical and preclinical imaging.](#) *Medical physics*, 42(8), pp.4796-4813.

mphDRR differs from X-ray forward projection, requiring multiplication by reciprocal squared distance from pinhole to source voxel

1.A.3. (Multiple-)pinhole collimators A pinhole collimator consists of a small pinhole aperture in a plate of lead, tungsten, or any other dense material [Figs. 2(c) and 1(d)]. The object of interest is projected through the aperture onto the detector. The most common pinhole has a knife-edge profile [Fig. 2(c)] but other shapes, e.g., channeled (keel-edge) pinholes, have also been used.⁴⁷ Keel-edge pinholes are particularly interesting for high-energy radionuclides and pinholes with large acceptance angles, as they reduce penetration. Other solutions to reduce penetration include the use of truncated pinholes⁴⁸ or clustered pinholes.⁴⁹

The resolution and sensitivity of a knife-edge pinhole collimator for a point source are⁵⁰

$$\text{Sens}_{\text{piho}}(h, \theta) = \frac{d_{\text{Seff}}^2 \sin^3 \theta}{16h^2}, \quad (8)$$

where θ and h determine the location of the point source in image space, with θ the angle of incidence measured from the plane of the pinhole aperture ($\theta = \pi/2$ for perpendicular incidence) and h the perpendicular distance from the point in the FOV to the plane defined by the pinhole aperture. d_{Seff} is the sensitivity-effective pinhole diameter, which is the physical pinhole diameter, d , corrected for penetration at the edges of the aperture at normal incidence,^{50,51}

Peterson, M., Gustafsson, J. and Ljungberg, M., 2017. Monte Carlo-based quantitative pinhole SPECT reconstruction using a ray-tracing back-projector. *EJNMMI physics*, 4, pp.1-21.

The line from the source volume origin through the pinhole centre is referred to as the pinhole axis, and the direction of the pinhole axis is specified by a polar angle θ and an azimuthal angle φ . The coordinates of **D** are calculated from those of **P** using the detector-to-pinhole distance **H** and origin-to-pinhole distance **R**.

$$\begin{bmatrix} x' \\ y' \\ z' \end{bmatrix} = \begin{bmatrix} \cos \varphi & \sin \varphi \sin \theta & \sin \varphi \cos \theta \\ 0 & \cos \theta & -\sin \theta \\ -\sin \varphi & \cos \varphi \sin \theta & \cos \varphi \cos \theta \end{bmatrix} \begin{bmatrix} x \\ y \\ z \end{bmatrix},$$

The coordinates of **D** are calculated by mirroring and then scaling x' and y' by a magnification factor M :

$$x_D = -Mx', \quad (4)$$

$$y_D = -My', \quad (5)$$

$$M = \frac{H}{R - z'}, \quad (6)$$

This is for a rotating mphSPECT system, but we use a similar mapping and make the same approximations

Due to the finite size of the source voxels, photons originating from a single voxel can contribute to several projection bins. This behaviour is modelled by adapting a

model includes several approximations. These are that (a) no attenuation or scatter occurs in the object, (b) the pinhole aperture opening is infinitely small without penetration effects (i.e. perfect collimation), and (c) the efficiency is independent of the incident angle.

Bronnikov, A.V., 2000. [A filtering approach to image reconstruction in 3D SPECT](#). *Physics in Medicine & Biology*, 45(9), p.2639.

$\mathbf{r} = (x, y, z)^T$. We assume that the attenuator is given by constant μ inside a convex area with a known boundary. The boundary is represented by vector function $\mathbf{b} \equiv \mathbf{b}(u, \theta) \in \mathbb{R}^3$ describing the intersection of the integration line with the surface of the attenuator facing the detector (see figure 1). Our mathematical model of the measured data g can be seen as a modification of the divergent beam transform of function f :

$$g(u, \theta) = e^{-\mu|\mathbf{b}|} \int_{-\infty}^{\infty} e^{\mu t} f(\mathbf{p} + t\mathbf{u}) dt \quad (3)$$

where the exponential factor in the integral is similar to that of the exponential Radon transform (see, for instance, Natterer (1986) for details of both transforms). Unlike the divergent beam transform (for $\mu = 0$), the integral (3) has a diverged kernel due to the presence of the factor $e^{\mu t}$, which complicates the reconstruction of function f . To derive our reconstruction algorithm, we resort to the representation of the line integral in \mathbb{R}^3 with the help of the line delta function. Thus, using

$$f(\mathbf{p} + t\mathbf{u}) = \int_{\mathbb{R}^3} f(\mathbf{r}) \delta(\mathbf{r} - \mathbf{p} - t\mathbf{u}) d\mathbf{r}$$

we obtain

$$\begin{aligned} g(u, \theta) &= e^{-\mu|\mathbf{b}|} \int_{-\infty}^{\infty} e^{\mu t} \int_{\mathbb{R}^3} f(\mathbf{r}) \delta(\mathbf{r} - \mathbf{p} - t\mathbf{u}) d\mathbf{r} dt \\ &= e^{-\mu|\mathbf{b}|} \int_{\mathbb{R}^3} e^{\mu(\mathbf{r}-\mathbf{p}) \cdot \mathbf{u}} \int_{-\infty}^{\infty} \delta(\mathbf{r} - \mathbf{p} - t\mathbf{u}) dt f(\mathbf{r}) d\mathbf{r}. \end{aligned} \quad (4)$$

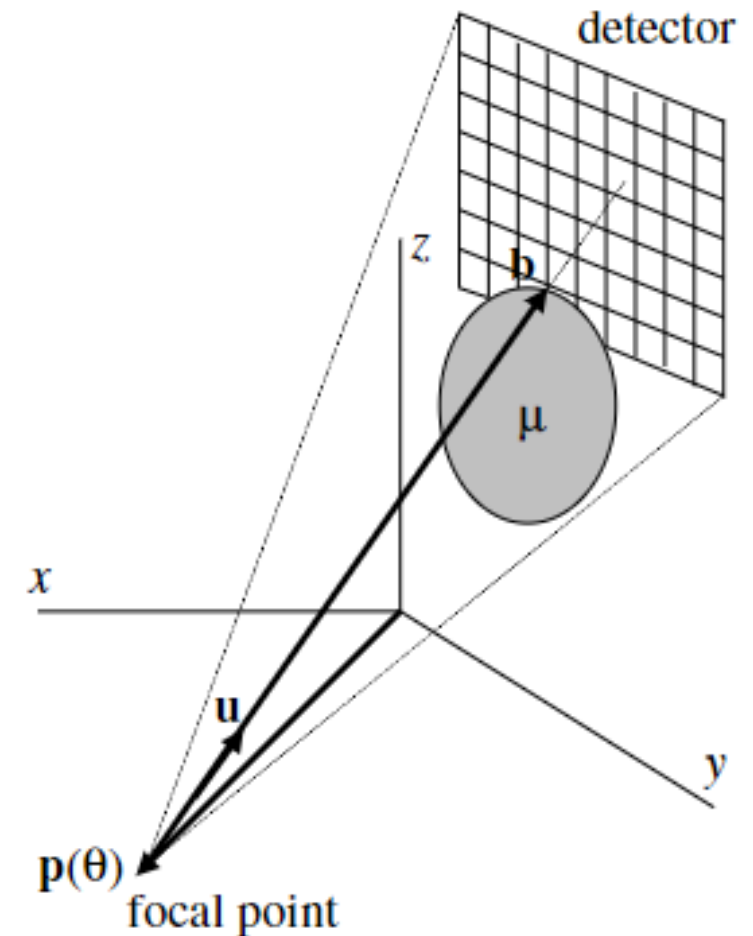


Figure 1. Geometry of 3D cone-beam SPECT imaging.

We will ignore attenuation, planning to use PyTomography method of co-registering with dual-energy CT and modeling attenuation at SPECT energies

Gopalakrishnan, V. and Golland, P., 2022, September. [Fast auto-differentiable digitally reconstructed radiographs for solving inverse problems in intraoperative imaging](#). In *Workshop on Clinical Image-Based Procedures* (pp. 1-11). Cham: Springer Nature Switzerland.

mphDRR differs from X-ray forward projection in requiring multiplication of voxel source intensity by reciprocal of squared pinhole source to voxel distance

2.1 DRR Generation

The process of generating a DRR models the geometry of an idealized projectional radiography system (Fig. 1a). Let $\mathbf{s} \in \mathbb{R}^3$ be the X-ray source, and $\mathbf{p} \in \mathbb{R}^3$ be a target pixel on the detector plane. Then $R(\alpha) = \mathbf{s} + \alpha(\mathbf{p} - \mathbf{s})$ is a ray that originates from \mathbf{s} ($\alpha = 0$), passes through the imaged volume, and hits the detector plane at \mathbf{p} ($\alpha = 1$). The total energy attenuation experienced by the X-ray by the time it reaches pixel \mathbf{p} is given by the following line integral:

$$E(R) = \|\mathbf{p} - \mathbf{s}\|_2 \int_0^1 \mathbf{V}(\mathbf{s} + \alpha(\mathbf{p} - \mathbf{s})) d\alpha \frac{d_{\text{Seff}}^2 \sin^3 \theta}{16h^2} \quad (1)$$

where $\mathbf{V} : \mathbb{R}^3 \mapsto \mathbb{R}$ is the imaged volume. The term $\|\mathbf{p} - \mathbf{s}\|_2$ endows the unit-free $d\alpha$ with the physical unit of length. For DRR synthesis, \mathbf{V} is approximated by a discrete 3D CT volume, and Eq. (1) becomes

$$E(R) = \|\mathbf{p} - \mathbf{s}\|_2 \sum_{m=1}^{M-1} (\alpha_{m+1} - \alpha_m) \mathbf{V} \left[\mathbf{s} + \frac{\alpha_{m+1} + \alpha_m}{2} (\mathbf{p} - \mathbf{s}) \right] \frac{d_{\text{Seff}}^2 \sin^3 \theta}{16h^2}$$

where α_m parameterizes the locations where ray R intersects one of the orthogonal planes comprising the CT volume, and M is the number of such intersections (Fig. 1b). Note that this model does not account for patterns of reflection and scattering that are present in real X-ray systems. While these simplifications

Gopalakrishnan, V. and Golland, P., 2022, September. [Fast auto-differentiable digitally reconstructed radiographs for solving inverse problems in intraoperative imaging.](#) In *Workshop on Clinical Image-Based Procedures* (pp. 1-11). Cham: Springer Nature Switzerland.

mphDRR does NOT differ from X-ray forward projection in the generation of Siddon coefficients, just in their application in a modified Eq. (2)

2.2 Siddon's Method and Its GPU Extensions

Siddon's method [10] provides a parametric method to identify the plane intersections $\{\alpha_m\}_{m=1}^M$. Let ΔX be the CT voxel size in the x -direction and b_x be the location of the 0-th plane in this direction. Then the intersection of ray R with the i -th plane in the x -direction is given by

$$\alpha_x(i) = \frac{b_x + i\Delta X - \mathbf{s}_x}{\mathbf{p}_x - \mathbf{s}_x}, \quad (3)$$

with analogous expressions for $\alpha_y(\cdot)$ and $\alpha_z(\cdot)$. We can use Eq. (3) to compute the values α_x for all the intersections between R and the planes in the x -direction:

$$\alpha_x = \{\alpha_x(i_{\min}), \dots, \alpha_x(i_{\max})\},$$

where i_{\min} and i_{\max} denote the first and last intersections of R with the x -direction planes. Defining α_y and α_z analogously, we construct the array

$$\alpha = \text{sort}(\alpha_x, \alpha_y, \alpha_z), \quad (4)$$

which contains M values of α parameterizing the intersections between R and the orthogonal x -, y -, and z -directional planes. We substitute values in the sorted set α into Eq. (2) to evaluate $E(R)$, which corresponds to the intensity of pixel \mathbf{p} in the synthesized DRR.

A faster variant determines consecutive intersecting planes iteratively [4]. For example, the value of α at the second plane intersected by R is given by $\alpha_2 = \min\{\alpha_x(i_{\min} + 1), \alpha_y(j_{\min} + 1), \alpha_z(k_{\min} + 1)\}$. The algorithm iteratively finds the next value of α until we reach the edge of the CT volume, making this approach more memory efficient by requiring fewer intermediate values to be stored. This modified algorithm, known as Siddon-Jacobs' method, is commonly implemented in CUDA and C++ to create multi-threaded GPU-accelerated DRR generators that exploit data parallelism by assigning each thread to trace an independent ray intersecting the detector plane [1,5,7].

2.3 Vectorizing Siddon's Method

While Siddon-Jacobs' method is more memory efficient, the iterative loop it relies on is not amenable to implementations in vectorized tensor algebra libraries. Thus we vectorize the original Siddon's method as follows. Let $\mathbf{P} \in \mathbb{R}^{H \times W \times 3}$ contain the 3D pixel coordinates of a DRR with dimension $H \times W$. We compute

the α values for intersections with all of the x -, y -, and z -planes for all $\mathbf{p} \in \mathbf{P}$ in parallel:

$$\mathbf{A} = \left(\begin{pmatrix} b_x \\ b_y \\ b_z \end{pmatrix} + \begin{pmatrix} i \\ j \\ k \end{pmatrix} \otimes \begin{pmatrix} \Delta X \\ \Delta Y \\ \Delta Z \end{pmatrix} - \mathbf{s} \right) \oslash (\mathbf{P} - \mathbf{s}) \in \mathbb{R}^{H \times W \times (n_x + n_y + n_z)}, \quad (5)$$

where (n_x, n_y, n_z) are the dimensions of the CT volume \mathbf{V} , (i, j, k) are the CT voxel indices, $(\Delta X, \Delta Y, \Delta Z)$ are the CT voxel sizes, and \otimes and \oslash are the Hadamard product and division operators, respectively. Rather than explicitly compute the indices (i_{\min}, i_{\max}) , (j_{\min}, j_{\max}) , and (k_{\min}, k_{\max}) for each ray, as is done in Siddon's original method, we instead compute the minimum and maximum values of α , corresponding to when each ray enters and exits the volume:

Gopalakrishnan, V. and Golland, P., 2022, September. [Fast auto-differentiable digitally reconstructed radiographs for solving inverse problems in intraoperative imaging](#). In *Workshop on Clinical Image-Based Procedures* (pp. 1-11). Cham: Springer Nature Switzerland.

mphDRR does NOT differ from X-ray forward projection in the generation of Vectorized Siddon coefficients, just in their application in a modified Eq. (2)

$$\alpha_{\min} = \max \{ \min\{\alpha_x(0), \alpha_x(n_x)\}, \min\{\alpha_y(0), \alpha_y(n_y)\}, \min\{\alpha_z(0), \alpha_z(n_z)\} \}$$

$$\alpha_{\max} = \min \{ \max\{\alpha_x(0), \alpha_x(n_x)\}, \max\{\alpha_y(0), \alpha_y(n_y)\}, \max\{\alpha_z(0), \alpha_z(n_z)\} \},$$

where $\alpha_{\min}, \alpha_{\max} \in \mathbb{R}^{H \times W}$. We filter \mathbf{A} to include only values in the range $[\alpha_{\min}, \alpha_{\max}]$ and sort each row $\mathbf{A}(h, w, \cdot)$ for $h \in \{1, \dots, H\}, w \in \{1, \dots, W\}$. Finally, we evaluate Eq. (2) with this sorted tensor to compute the intensity for each pixel in the DRR, completing a chain of vectorized tensor operations.

Because we reformulated the original Siddon's method as a series of tensor operations, our vectorized version benefits from the mature GPU compilers and memory allocators developed for optimizing large-scale deep learning models. For empirical evaluation of our method, we also implemented a partially-vectorized version of Siddon-Jacobs' method in which the α updates are still computed iteratively (i.e., with a loop), but the updates are applied in a vectorized form to every target pixel in the detector plane.

Nguyen, M.P., Goorden, M.C., Ramakers, R.M. and Beekman, F.J., 2021. [Efficient Monte-Carlo based system modelling for image reconstruction in preclinical pinhole SPECT](#). *Physics in Medicine & Biology*, 66(12), p.125013.

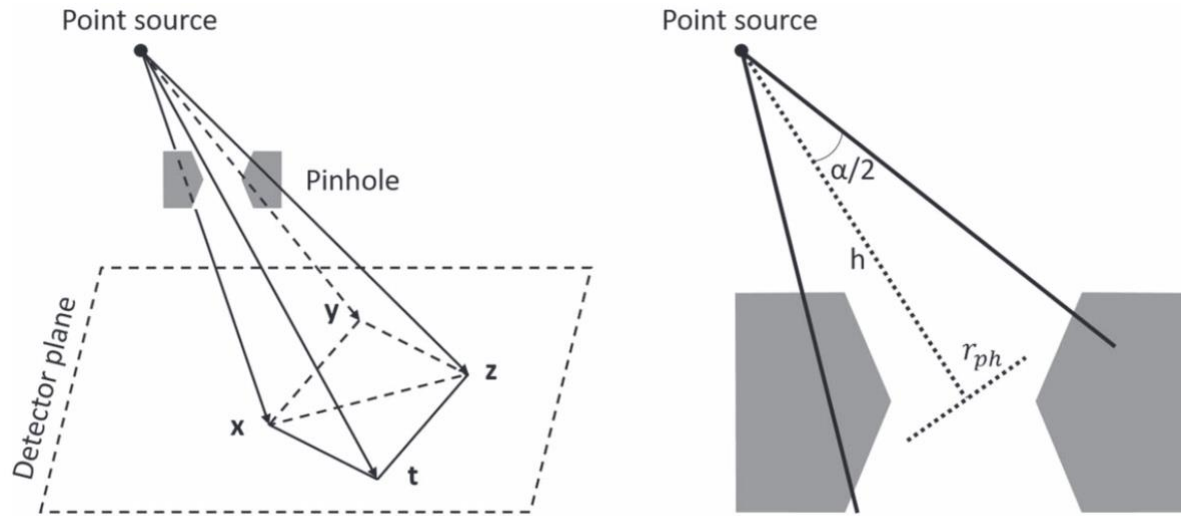


Figure 1. Accelerated point source simulation by forced irradiation from the point source to each pinhole.

We have been using a similar method to speed our GATE simulations.

We can learn from GATE system models.

2.3.2. Accelerated point source simulation This step is the key that allows for the accurate generation of PSFs for the radionuclide of interest based on MCS without additional measurements. In this simulation, an infinitely small point source was defined in GATE, with the same set of point source positions as in the calibration measurement being used. The point source was assumed to be in water. A simple acceleration technique was applied for the point source simulation by **directing the photon emission from the point source to the pinholes in narrow beams** instead of the default emission at all angles. This is a kind of forced detection—one of the variance reduction techniques in MCS. There exist several implementations of forced detection for pinhole SPECT (Gieles et al 2002, Beenhouwer and Staelens 2010). In our method, only the emission angle from the decay location at the point source is adjusted, and no alteration is applied at individual photon interaction points as in the other methods, meaning it is simple to implement in GATE at the macro level just by setting the span of the polar angle and the azimuthal angle of the emission distribution. Note that this acceleration technique was used for a point source, but it was not suitable for large sources and hence not used for the studied scans in section 2.4. In our acceleration technique, the photon beams were adapted for each point source and pinhole combination.

Huang, P.C., Hsu, C.H., Hsiao, I.T. and Lin, K.M., 2009. [An accurate and efficient system model of iterative image reconstruction in high-resolution pinhole SPECT for small animal research.](#) *Journal of Instrumentation*, 4(06), p.P06007.

B. Ideal Pinhole

For an ideal pinhole in Fig. 1 (a), the pinhole collimator has an infinitely small aperture. We assume that an incident photon will be detected by four neighboring detectors as shown in Fig. 2. For a detector, the probability value to detect a photon is assumed to be inversely proportional to the distance between the incident photon and the detector center. Fig. 2 shows an example of a photon detection by four detectors. The probability values of photon detection are computed as follows:

$$\begin{aligned} P_A &= \frac{bcd}{abc + abd + acd + bcd} \\ P_B &= \frac{acd}{abc + abd + acd + bcd} \\ P_C &= \frac{abd}{abc + abd + acd + bcd} \\ P_D &= \frac{abc}{abc + abd + acd + bcd} \end{aligned} \quad (4)$$

where P_A , P_B , P_C , and P_D are the probabilities corresponding to detectors A, B, C, and D, respectively.

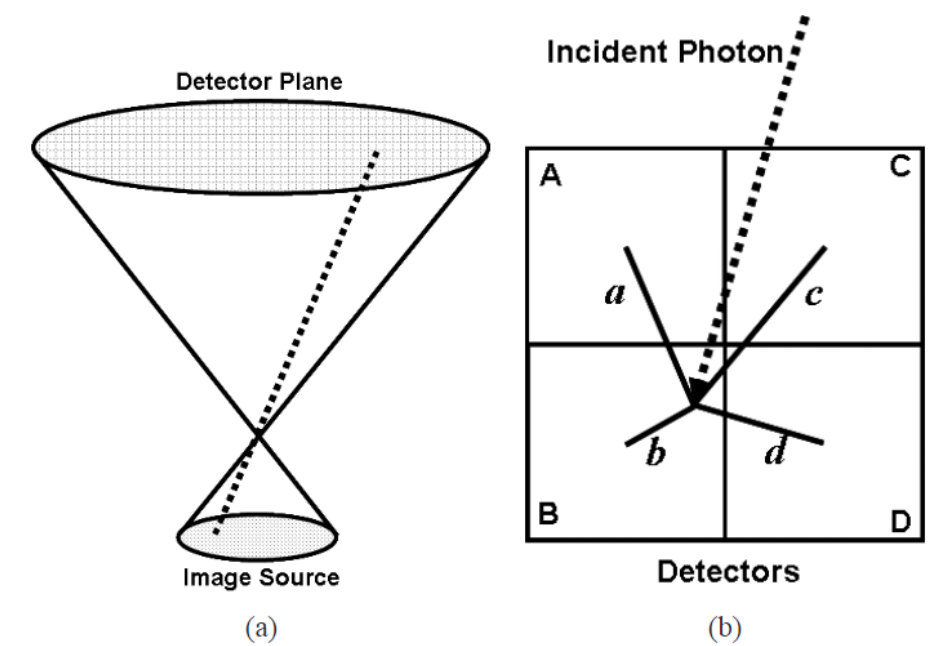


Figure 1. (a) Ideal pinhole aperture. (b) Photon detection model for ideal pinhole: the probability of detecting a photon is inversely proportional to the distance between the incident photon and the center of the detector.

Simple methods exist for modeling PSF effects from detector coordinate discretization and finite-size pinholes

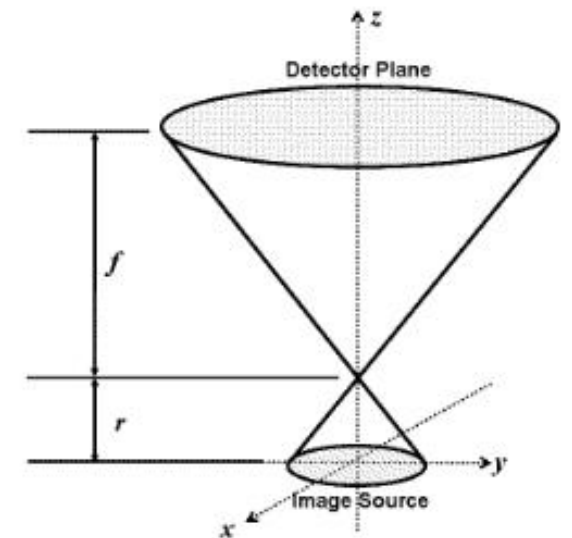
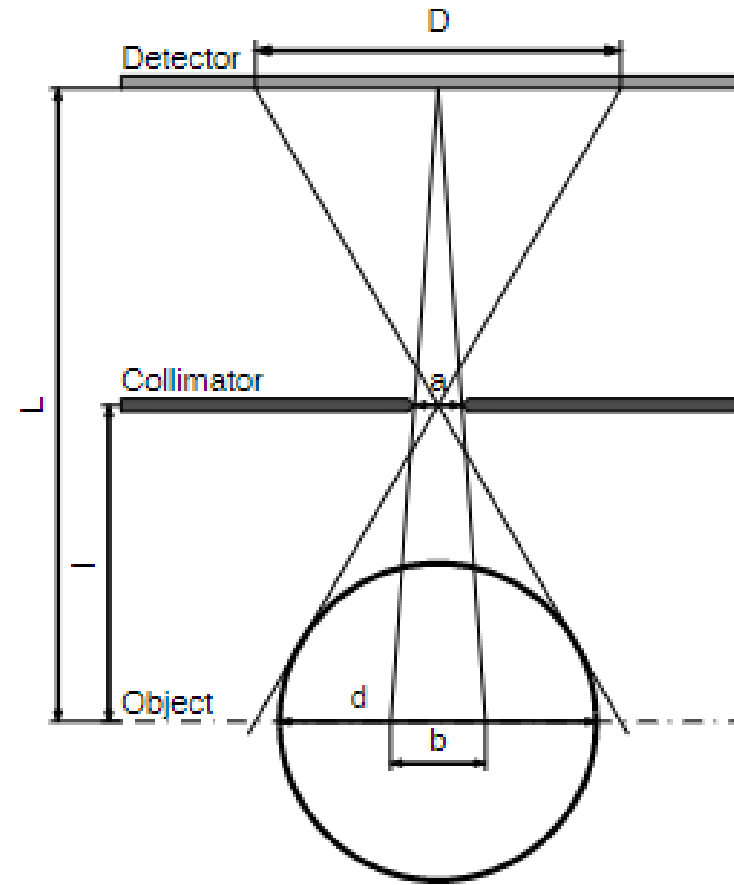


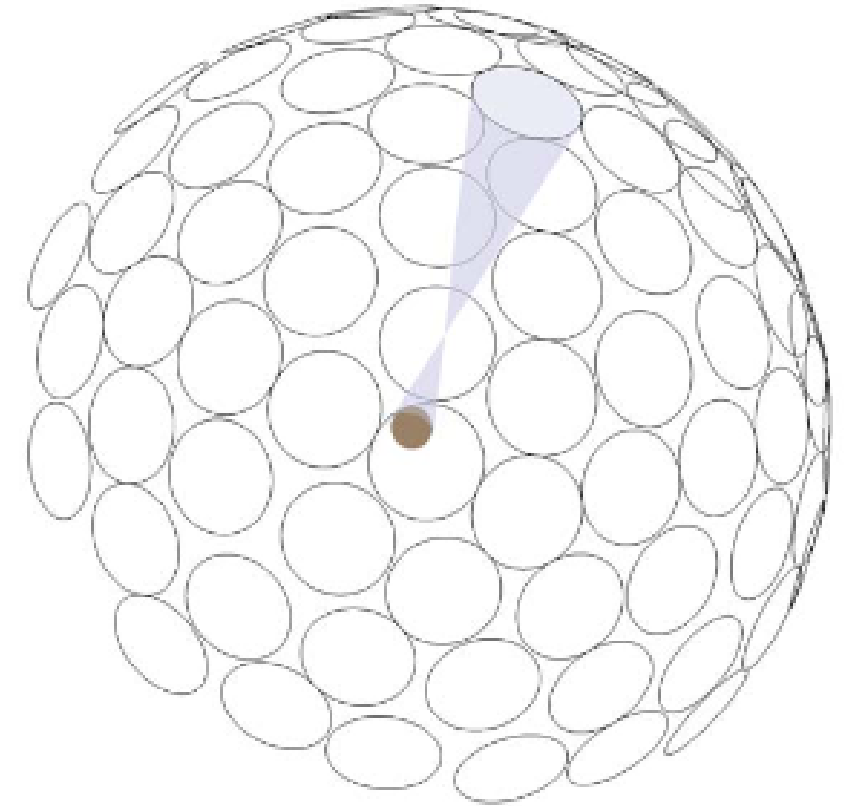
Fig. 4. Configuration of a pinhole system

Nillius, P. and Danielsson, M., 2008, October. [Theoretical bounds and optimal configurations for multi-pinhole SPECT](#). In *2008 IEEE Nuclear Science Symposium Conference Record* (pp. 5020-5022). IEEE.

This work describes
multi-pinhole SPECT
system design issues
more generally



(a)



(b)

Fig. 1. Multi-pinhole camera geometry. (a) Single pinhole geometry. (b) In multi-pinhole cameras the images of the pinholes have to fit onto the detector sphere without overlap.